TOPICAL REVIEW — Topological insulator

From magnetically doped topological insulator to the quantum anomalous Hall effect*

He Ke(何 珂)[a)†], Ma Xu-Cun(马旭村)[a)], Chen Xi(陈 曦)[b)], Lü Li(吕 力)[a)], Wang Ya-Yu(王亚愚)[b)‡], and Xue Qi-Kun(薛其坤)[b)§]

[a)] *Beijing National Laboratory for Condensed Matter Physics, Institute of Physics, Chinese Academy of Sciences, Beijing* 100190, *China*
[b)] *State Key Laboratory of Low-Dimensional Quantum Physics, Department of Physics, Tsinghua University, Beijing* 100084, *China*

(Received 16 May 2013)

Quantum Hall effect (QHE), as a class of quantum phenomena that occur in macroscopic scale, is one of the most important topics in condensed matter physics. It has long been expected that QHE may occur without Landau levels so that neither external magnetic field nor high sample mobility is required for its study and application. Such a QHE free of Landau levels, can appear in topological insulators (TIs) with ferromagnetism as the quantized version of the anomalous Hall effect, i.e., quantum anomalous Hall (QAH) effect. Here we review our recent work on experimental realization of the QAH effect in magnetically doped TIs. With molecular beam epitaxy, we prepare thin films of Cr-doped $(Bi,Sb)_2Te_3$ TIs with well-controlled chemical potential and long-range ferromagnetic order that can survive the insulating phase. In such thin films, we eventually observed the quantization of the Hall resistance at h/e^2 at zero field, accompanied by a considerable drop in the longitudinal resistance. Under a strong magnetic field, the longitudinal resistance vanishes, whereas the Hall resistance remains at the quantized value. The realization of the QAH effect provides a foundation for many other novel quantum phenomena predicted in TIs, and opens a route to practical applications of quantum Hall physics in low-power-consumption electronics.

Keywords: topological insulator, quantum anomalous Hall effect, quantum Hall effect, ferromagnetic insulator, molecular beam epitaxy

PACS: 73.21.Fg, 73.43.–f, 75.50.Pp, 75.70.–i **DOI:** 10.1088/1674-1056/22/6/067305

1. Introduction

Electrons in the microscopic world, for example in an atom, can travel without losing their energy by small perturbations. It is one of the most amazing manifestations of quantum mechanics laws.[1] If the dissipationless nature of electrons could be kept in a macroscopic system, electronic devices with low energy-consumption could be expected. Quantum Hall effect (QHE) observed in two-dimensional (2D) electron systems represents one class of the quantum phenomena that appear in macroscopic scale.[2,3] In QHE, the Hall resistance, which is the voltage across the transverse direction of a conductor divided by the longitudinal current,[4] is quantized into plateaus of height h/ve^2, with h being Planck's constant, e the electron's charge, and v an integer[2] or a certain fraction.[3] At the same time the longitudinal resistance is significantly reduced, even to zero, resulting from the dissipationless electronic transport in QH states.

Conventional QHE is a consequence of the formation of Landau levels.[2] The magnetic field-induced Landau quantization drives a 2D electron system into an insulating phase that is topologically different from the vacuum and usual insulators.[5–7] Dissipationless QH edge states emerge as required by the change in topological character. Well-defined Landau levels are possible only in high-mobility samples under strong external magnetic fields. If a topologically nontrivial electronic structure can be realized without Landau levels, QHE is expected to be observed without external magnetic field and high sample mobility. This means applications of the novel QH physics are possible in practical electronic devices. Such an idea of QHE in the absence of Landau levels was first proposed in 1988 by F. D. M. Haldane in graphene model with the time reversal symmetry (TRS) broken by current loops.[8]

Besides the ordinary Hall effect (OHE) determined by charge carriers, a magnetic material also shows a strong Hall effect induced by magnetization, which is known as the "anomalous Hall effect" (AHE).[9] In a ferromagnetic film with perpendicular magnetic anisotropy, the AHE can be observed with no external magnetic field. It has been proposed that AHE in some magnetic materials is determined by the Berry curvature of the energy bands.[10] This so-called intrin-

*Project supported by the National Natural Science Foundation of China (Grant Nos. 11174343 and 11134008), the National Basic Research Program of China (Grant Nos. 2013CB921702 and 2009CB929400), and the Knowledge Innovation Program of the Chinese Academy of Sciences.

†Corresponding author. E-mail: kehe@iphy.ac.cn
‡Corresponding author. E-mail: yayuwang@mail.tsinghua.edu.cn
§Corresponding author. E-mail: qkxue@mail.tsinghua.edu.cn

sic AHE can be quantized in a 2D ferromagnetic material, known as the quantum anomalous Hall (QAH) effect, which also means QHE free of Landau levels.[10,11] However, although experimental evidence for intrinsic AHE has been reported many times,[10] little progress has been made toward the experimental realization of the QAH effect.

The discovery of time-reversal-invariant topological insulators (TIs),[12,13] partly inspired by F. D. M. Haldane's paper in 1988, gave new hope to the experimental realization of the QAH effect.[14,15] A TI also has topologically non-trivial electronic structure induced by spin–orbit coupling (SOC) of the material rather than external magnetic field. A 2D TI is expected to show the quantum spin Hall (QSH) effect, a time-reversal-invariant version of quantum Hall effect, in which a pair of spin-filtered and Dirac-type edge states contributes to quantized spin accumulation at the two edges and quantized longitudinal resistance.[16,17] The QSH effect has been experimentally observed in HgTe/CdTe[16,17] and InAs/GaSb/AlSb[18,19] quantum wells. A three-dimensional (3D) TI is a bulk insulator with 2D spin-split and Dirac-type surface states at each surface,[20] which was first found in Bi_xSb_{1-x} alloys.[21–23] The most familiar 3D TI materials by far are the Bi_2Se_3 family compounds: Bi_2Se_3, Bi_2Te_3, and Sb_2Te_3, for their ordered lattice structures, relatively large bulk gaps (up to 0.3 eV in Bi_2Se_3), and simple surface band structures.[24–27]

Breaking the TRS of a thin film of suitable TI, no matter whether it is a 2D or 3D TI, by introducing ferromagnetism can naturally lead to the QAH effect.[28–32] In a 2D TI, ferromagnetism can remove one of the pair of spin channels of the QSH edge states, changing the system into a QAH insulator.[29] Magnetization in a 3D TI opens a gap in the Dirac surface band at each surface perpendicular to the magnetization vector and drives it into a QH system with half quantum Hall conduction ($e^2/2h$) carried by the edge states at the domain wall.[30,32] In a perpendicularly magnetized 3D TI film, the gapped surface bands at top and bottom surfaces have different topological characters due to their opposite normal directions. Thus the sample edge acts as a domain wall between the two QH surface bands where both of the edge states are located and contribute to a total Hall conductance of e^2/h, which can be detected by contacts at the edge. The QAH effect can also be observed in a thin film of 3D TI with the Dirac surface states gapped by finite-size effect, unless the surface state gap is smaller than the ferromagnetic exchange energy.[31]

From the experimental point of view, to observe the QAH effect in a TI, one needs to do the following. First, introduce long-range ferromagnetic order into the TI. The ferromagnetism should be able to hold even in the insulating regime and have the easy magnetization axis perpendicular to the film plane. Second, prepare thin films of the TI material. The film should have uniform thickness and be as thin as possible, to promote localization of dissipative channels, unless the gap between the lowest order quantum well subbands (essentially the same as the gap opened at the Dirac surface states due to finite-size effect) is larger than the ferromagnetic exchange energy. Third, finely tune the Fermi level into the magnetically induced subband gap. In the QAH regime, one should expect to observe a plateau of Hall conductance (σ_{xy}) of e^2/h and a vanishing longitudinal conductance (σ_{xx}) even at zero magnetic field (see the schematic drawings in Fig. 1).[28–31]

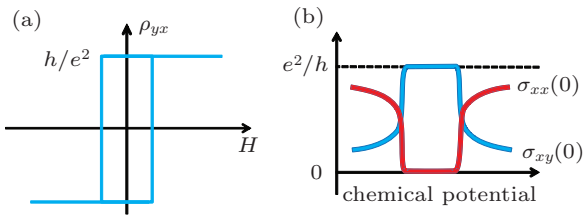

Fig. 1. Schematic drawings of the expected magnetic field (H) dependence of Hall resistance (ρ_{yx}) (a) and the chemical potential dependence of zero field σ_{xx} [$\sigma_{xx}(0)$, in red] and σ_{xy} [$\sigma_{xy}(0)$, in blue] in the QAH effect.

2. Material considerations

Bi_2Se_3, Bi_2Te_3, and Sb_2Te_3 are excellent 3D TI materials.[24] In our previous work, we successfully prepared high quality thin films of Bi_2Se_3 family TIs by molecular beam epitaxy (MBE) on various substrates.[33–36] The film thickness can be made uniform in macroscopic scale, and the size of the surface state gap can be well controlled by tuning the film thickness.[33,35,36] Such MBE-grown thin films of Bi_2Se_3 family TIs provides a perfect starting point to experimentally realize the QAH effect.

Another merit of the Bi_2Se_3 family TIs for realizing the QAH effect is that their unique band structure can support ferromagnetic insulator phase when doped with magnetic impurities.[31] In most conventional diluted magnetic semiconductors, the long-range ferromagnetic order is believed to be through RKKY-type ferromagnetic coupling between magnetic impurities far from each other, mediated by itinerant charge carriers.[37,38] Carriers of a certain density and type are required for the RKKY-type ferromagnetism, which therefore can never be expected to exhibit the QAH effect. Fortunately, in magnetically doped Bi_2Se_3 family TIs, thanks to the inverted band structure, bands above and below the bulk gap have similar electronic components, which leads to a rather large van Vleck magnetic susceptibility of valence electrons even when the Fermi level lies in the gap. Hence the spins of the magnetic impurities in Bi_2Se_3 family TIs can be ferromagnetically coupled by the large van Vleck susceptibility of

valence electrons, even in the insulating regime.

Of the three members of the Bi_2Se_3 family TIs, Bi_2Se_3 is naturally the first choice for its largest bulk gap and its Dirac point residing in the bulk gap. However we could not find long-range ferromagnetic order in magnetically doped Bi_2Se_3 down to 1.5 K.[39] One of the main problems that prevent long-range ferromagnetic order in magnetically doped Bi_2Se_3 lies in the fact that the SOC of $Bi_2Se_3$is mainly contributed by Bi atoms; therefore Cr substitution of Bi significantly reduces the SOC of the system so that the inverted band structure can be removed with the van Vleck susceptibility significantly weakened.[39] On the other hand, in Sb_2Te_3 and Bi_2Te_3, since Te atoms also contribute to significant SOC, the band structure and van Vleck susceptibility are little influenced by magnetic doping.[39,40] Indeed, ferromagnetism has been reported in Cr- and V-doped Sb_2Te_3[41] and Mn-doped Bi_2Te_3.[42] For MBE growth, Cr is a better choice for the magnetic impurities because it has relatively low evaporation temperature and high purity evaporant is easy to obtain.

Sb_2Te_3 and Bi_2Te_3 have the same crystal structure and close lattice constants, whereas the former is usually p-doped and the latter is usually n-doped.[43,44] One is able to tune the chemical potential by mixing the two compounds in certain ratio. In our previous work,[45] we obtained thin films of $(Bi,Sb)_2Te_3$ ternary compounds with well-controlled composition with MBE, and found that the topological surface states exist over the entire composition range with the carriers tunable between p- and n-type. Moreover, near the charge neutral point (CNP), the carrier density values estimated by ARPES and transport measurements are quite consistent. This suggests that $(Bi,Sb)_2Te_3$ is not so sensitive to ambient conditions as Bi_2Se_3 and has little band bending.[46] These properties are very important for systematic transport studies on TI films.

Due to the above considerations, we chose MBE-grown Cr-doped $(Bi,Sb)_2Te_3$ thin films as the material to realize the QAH effect.

3. Ferromagnetic insulator phase in magnetically doped TI

The MBE growth of Cr-doped $(Bi_xSb_{1-x})_2Te_3$ films was carried out in an ultrahigh vacuum (UHV) system (Omicron) with the base pressure $\sim 8 \times 10^{-11}$ mbar (1 bar = 10^5 Pa). The films were grown by co-evaporating Bi (99.9999%), Sb (99.9999%), Cr (99.999%), and Te (99.9999%) from standard Knudsen cells to commercial sapphire (0001) or $SrTiO_3$ (111) substrates. The growth was conducted under Te-rich conditions at a substrate temperature of $\sim$ 180 °C with a typical Te/(Bi,Sb) flux ratio of 10. The typical growth rate was about 0.125 QL/minute. The MBE chamber is connected to an analysis chamber equipped with scanning tunneling microscope (STM) and angle-resolved photoemission spectroscopy (ARPES) system, which enables *in situ* characterization of atomic and electronic structures.[40]

Figure 2(a) shows a typical STM image of the surface morphology of a $Cr_{0.22}Sb_{1.78}Te_3$ film. Atomically flat terraces are observed in large scale without traces of clusters or inhomogeneous regions, which indicates uniform distribution of Cr atoms in the Sb_2Te_3 matrix. Cr impurities manifest themselves in STM images as randomly distributed triangle-shaped dark features on the surface, as shown in Fig. 2(b). Each triangle is composed of three dark spots on the positions of the topmost Te atoms (see the high-resolution image in the inset of Fig. 2(b)). However, since all the triangles point to the same direction, they are unlikely Cr "trimers" but single Cr atoms occupying subsurface Sb sites, reducing the local density of states of the three Te atoms above (see the structural model shown in Fig. 2(c)).

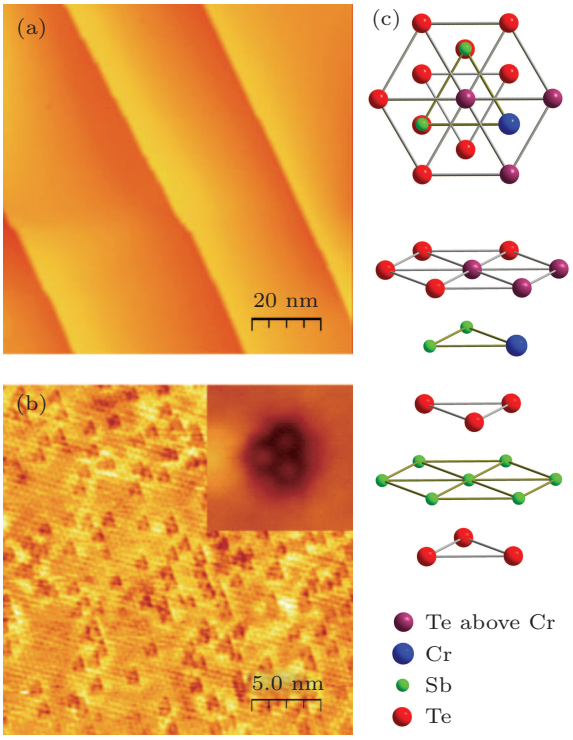

Fig. 2. Surface morphology and structure of Cr-doped Sb_2Te_3. (a) STM image (100 nm × 100 nm) of the surface morphology of $Cr_{0.22}Sb_{1.78}Te_3$. (b) STM image (25 nm × 25 nm) showing Cr impurities in Sb_2Te_3 matrix. The inset displays a high-resolution STM image near a single Cr impurity. (c) Atomic structural model indicating the position of a Cr impurity in Sb_2Te_3 lattice.[40]

Figures 3(a)–3(e) display the ARPES bandmaps (the 2nd differentiated data) of a pure Sb_2Te_3 film and four $Cr_{0.22}(Bi_xSb_{1-x})_{1.78}Te_3$ films with systematically varied Bi:Sb ratios measured at room temperature. The corresponding momentum distribution curves (MDCs) are displayed in Figs. 3(f)–3(j). The two linearly dispersed bands crossing the

Fermi level shown in the spectra for Sb_2Te_3 are Dirac surface bands (Figs. 3(a) and 3(f)).[36] The Dirac point is located above the Fermi level, due to *p*-doping of native Sb_2Te_3. After doping Cr impurities, even to a rather high level ($> 10\%$ of cations in the present data), the Dirac surface bands can still be clearly resolved, with the band dispersion little modified (Figs. 3(b) and 3(g)) and the hole density increased. Doping Bi also has little influence on the band dispersion of the Dirac surface states, as shown in the spectra for all the Bi contents used. On the other hand, the Fermi level is shifted upward with increasing Bi content, from below the Dirac point (Figs. 3(c) and 3(h)) for $x = 0.1$), to near the CNP (Figs. 3(d) and 3(i) for $x = 0.25$), and then to above the Dirac point (Figs. 3(e) and 3(j) for $x = 0.4$).[45] The existence of Dirac surface bands in all the samples suggests that the materials are still 3D TIs even at such a high Cr doping level, without experiencing any topological phase transition like that in Cr-doped Bi_2Se_3.[39] Magnetically induced gap-opening at the Dirac point is not observed, since the TRS still holds in paramagnetic phase at the measurement temperature (room temperature).

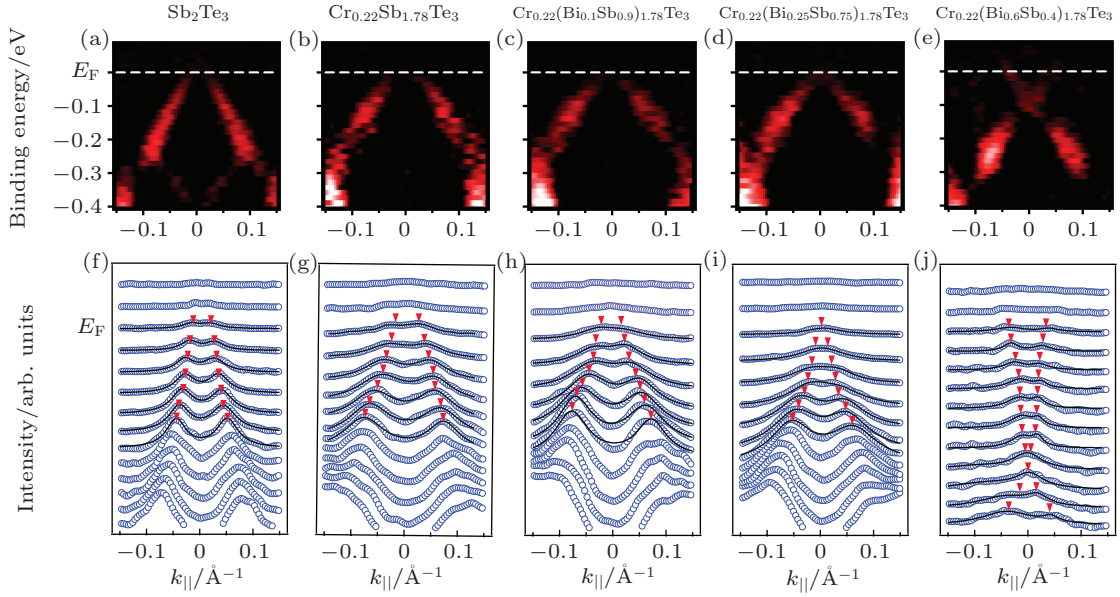

Fig. 3. (a)–(e) ARPES grey-scale bandmaps of an Sb_2Te_3 film (a) and the $Cr_{0.22}(Bi_xSb_{1-x})_{1.78}Te_3$ films with $x = 0$ (b), $x = 0.1$ (c), $x = 0.25$ (d), and $x = 0.6$ (e). (f)–(j) ARPES MDCs corresponding to panels (a)–(e). In panels (f)–(j), the blue empty circles are data points; the black solid lines are results of fitting with double Lorentz peak; the red triangles indicate the fitted peak positions.[40]

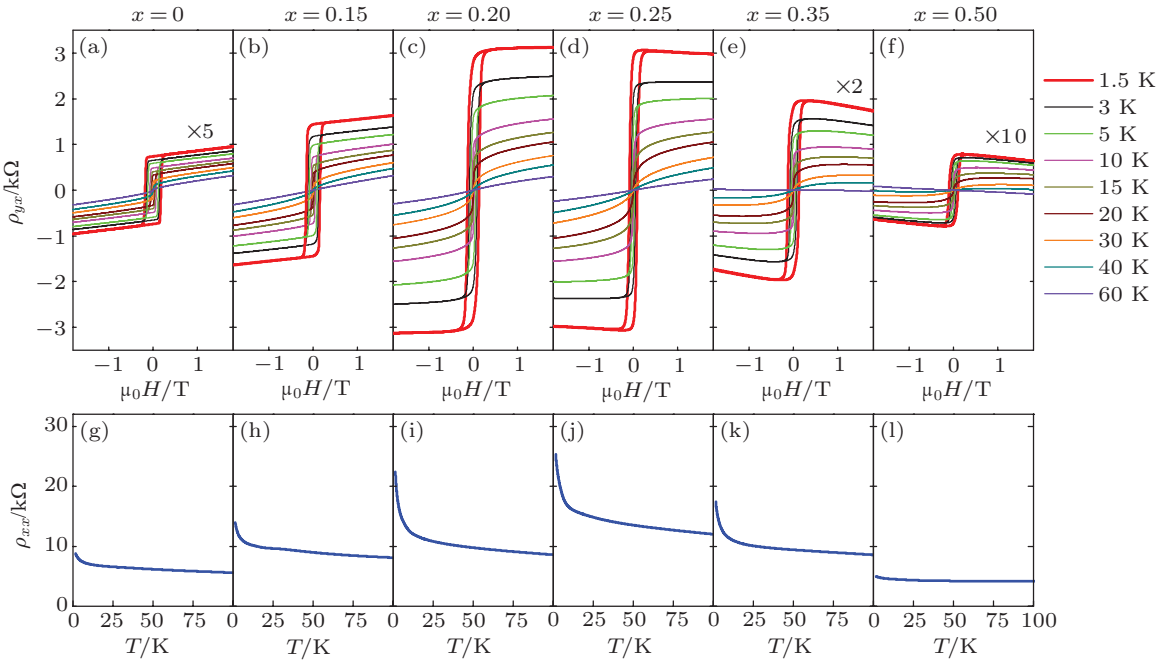

Fig. 4. Transport properties of Cr-doped $(Bi_xSb_{1-x})_2Te_3$ films. (a)–(f) Magnetic field-dependent Hall resistance ρ_{yx} of the $Cr_{0.22}(Bi_xSb_{1-x})_{1.78}Te_3$ films with $x = 0$ (a), $x = 0.15$ (b), $x = 0.2$ (c), $x = 0.25$ (d), $x = 0.35$ (e), and $x = 0.5$ (f) at different temperatures. (g)–(l) Temperature-dependent longitudinal resistance ρ_{xx} of the films with $x = 0$ (g), $x = 0.15$ (h), $x = 0.2$ (i), $x = 0.25$ (j), $x = 0.35$ (k), and $x = 0.5$ (l).[40]

Transport properties of the 5 QL $Cr_{0.22}(Bi_xSb_{1-x})_{1.78}Te_3$ films are measured in the Hall bar geometry with the AC lock-in method. Figure 4 shows the transport data of 5 QL $Cr_{0.22}(Bi_xSb_{1-x})_{1.78}Te_3$ films grown on sapphire (0001) substrates with different Bi contents. The upper panels (Figs. 4(a)–4(f)) display the magnetic field ($\mu_0 H$)-dependent Hall resistance (ρ_{yx}) measured at different temperatures (down to 1.5 K). The lower ones (Figs. 4(g)–4(l)) display the temperature-dependent longitudinal resistance (ρ_{xx}). For all the films, the ρ_{yx}–$\mu_0 H$ curves measured at 1.5 K (the thicker ones in Figs. 4(a)–4(f)) show nearly square-shaped hysteresis loops at low field, suggesting good long-range ferromagnetic order with the easy magnetization axis perpendicular to the sample plane.[10] Meanwhile with increasing Bi content (x), the slope of the linear background at high field evolves from positive to negative, indicating the change of the dominating carriers from p- to n-type at around $x = 0.2 \sim 0.25$, consistent with the above ARPES observations. The temperature-dependent ρ_{xx} curves of all the films (Figs. 4(g)–4(l)) exhibit a typical insulating behavior. Among them the samples with $x = 0.2$ and 0.25 show the largest values, both exceeding 20 kΩ at 1.5 K, which can be attributed to their low carrier densities near the p–n crossover region. So the ferromagnetism of Cr-doped $(Bi_xSb_{1-x})_2Te_3$ always holds despite the significant change in carrier density and type induced by different Bi concentrations. The ferromagnetism has also been confirmed by direct magnetization measurements with SQUID magnetometer, which shows hysteresis loops similar with those of AHE. The magnetic moment per Cr ion, estimated from the SQUID data, is $\sim 3\ \mu_B$, which is basically that of a Cr^{3+} ion and varies little with Bi content. The moment value is quite reasonable since 3+ is the most stable oxidation state of Cr.

We can estimate the Curie temperatures (T_Cs) of the $Cr_{0.22}(Bi_xSb_{1-x})_{1.78}Te_3$ films through temperature-dependent AH resistance, defined as ρ_{yx} at zero field ($\rho_{yx}(0)$), which reflects the spontaneous magnetization of the samples. Figure 5(a) is a plot of the T_Cs of the samples of different Bi contents. The corresponding carrier densities estimated by the OHE are shown as the tick labels of the top axis. We can see that T_C varies little with carrier density and type, always being around 30 K $\sim$ 35 K, even in the rather insulating samples around the p–n crossover region (blue area), which clearly indicates carrier independence of the ferromagnetism.

The AH resistance, on the other hand, exhibits a dramatic and systematic change with Bi doping. $\rho_{yx}(0)$ is only 148 Ω at 1.5 K for the $x = 0$ sample but abruptly increases to 1.4 kΩ about one order of magnitude larger for the $x = 0.15$ sample. The value is further enhanced to 2.8 kΩ at $x = 0.2$, and 2.9 kΩ at $x = 0.25$, respectively. But as x reaches 0.35, $\rho_{yx}(0)$ rapidly drops to 900 Ω, and then to only 72 Ω at $x = 0.5$. The evolution of $\rho_{yx}(0)$ with Bi content and carrier density is summarized in Fig. 5(b). A maximum occurs near the p–n crossover region (blue area), with $\rho_{yx}(0)$ about 40 times larger than the minimum value. Evolution of zero field ρ_{xx} ($\rho_{xx}(0)$) with Bi content is also plotted here, exhibiting a similar maximum with ρ_{AH}, but with smaller relative variation than that of $\rho_{yx}(0)$. The $\rho_{yx}(0)/\rho_{xx}(0)$ ratio, i.e. tangent of the AH angle, is only about 0.02 for high carrier density samples but increases by more than 5 times near the crossover region.

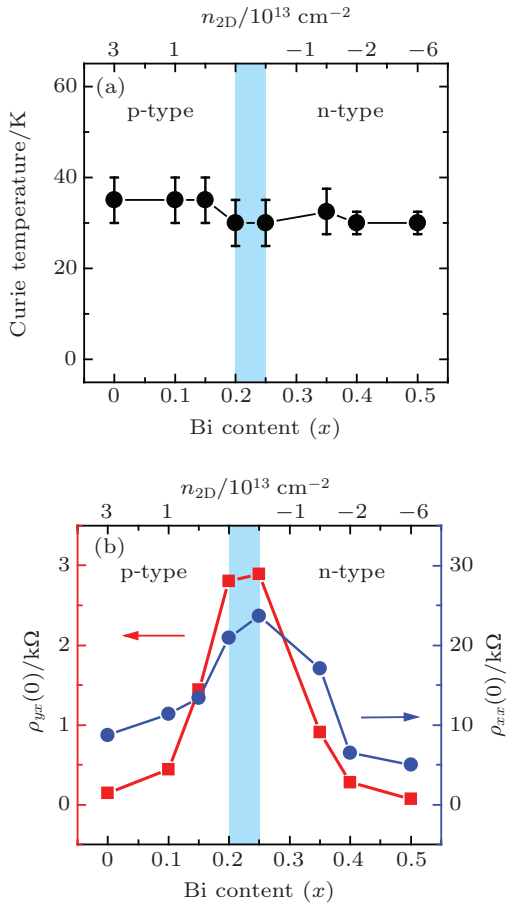

Fig. 5. (a) Dependence of Curie temperature (T_C) on Bi content (x) (bottom axis) and carrier density (top axis). Error bars represent the temperature spacing in $\rho_{yx}(0)$–T measurements. (b) Dependence of $\rho_{yx}(0)$ (red solid squares) and $\rho_{xx}(0)$ (blue solid circles) at 1.5 K on Bi content (x) (bottom axis) and carrier density (top axis).[40]

Only by varying the Bi:Sb ratio it is difficult to tune the carrier density to a very low value. Electric field effect has to be applied to realize accurate tuning of the chemical potential. $SrTiO_3$ has a huge dielectric constant ($\sim 2 \times 10^4$) at low temperature. By using $SrTiO_3$ as the substrate to grow Cr-doped $(Bi,Sb)_2Te_3$ film, one can realize carrier density variation of $\sim 3 \times 10^{13}$ cm^{-2} with back-gate voltage (V_g) between ±210 V for a typical substrate thickness of 0.5 mm (see the schematic drawing for measurement setup with $SrTiO_3$ substrate as gate dielectric in Fig. 6(a)).[47] Figure 6(b) shows

the ρ_{yx} hysteresis loops of a 5-QL $Cr_{0.22}(Bi_{0.2}Sb_{0.8})_{1.78}Te_3$ film grown on $SrTiO_3$ (111) measured at 250 mK with different V_gs. $\rho_{yx}(0)$ changes dramatically with V_g, from 660 Ω at −210 V to 6.1 kΩ (the maximum) at 35 V, as summarized in Fig. 6(c). ρ_{xx} also exhibits a peak of ∼30 kΩ at 80 V. The maximum $\rho_{yx}(0)/\rho_{xx}(0)$ ratio reaches ∼ 0.2, indicating an unusually large AH effect. The coercivity and the shape of the hysteresis loops are nearly unchanged with V_g, suggesting that the variation in carrier density has little influence on the ferromagnetism.

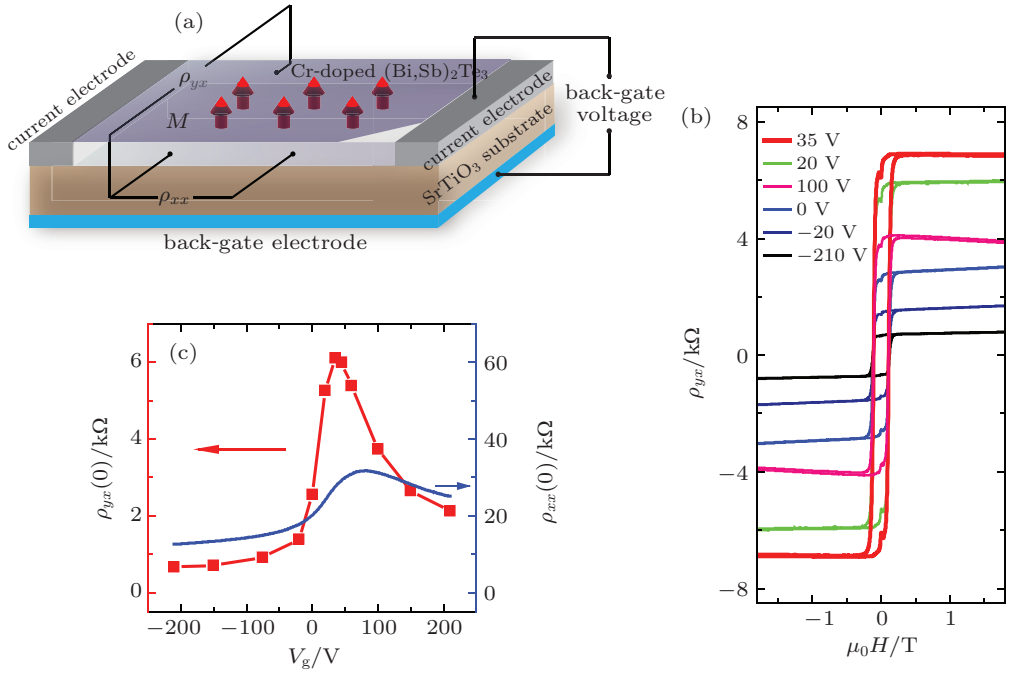

Fig. 6. (a) A schematic drawing depicting measurement geometry of back-gated Cr-doped $(Bi,Sb)_2Te_3$ film with $SrTiO_3$ substrate as gate dielectrics. (b) Magnetic field-dependent ρ_{yx} of a 5-QL $Cr_{0.22}(Bi_{0.2}Sb_{0.8})_{1.78}Te_3$ film grown on $SrTiO_3$ (111) substrate at different V_gs measured at 250 mK. (c) Dependence of $\rho_{yx}(0)$ (red solid squares) and $\rho_{xx}(0)$ (blue solid line) of the 5-QL $Cr_{0.22}(Bi_{0.2}Sb_{0.8})_{1.78}Te_3$ film grown on $SrTiO_3$ (111) substrate on V_g at 250 mK.[40]

Hence both composition and gate-voltage-dependent experiments have demonstrated robust long-range ferromagnetic order in thin films of Cr-doped $(Bi,Sb)_2Te_3$ against the variation in both carrier density and type, consistent with the van Vleck susceptibility-mediated ferromagnetism.[31] So the ferromagnetic insulator phase, can indeed be realized in Cr-doped $(Bi,Sb)_2Te_3$ thin films, which promises the appearance of the QAH effect in them.

4. Observation of the QAH effect

Although in the above work, ferromagnetic insulator phase has been realized and a significant increase of AH resistance with decreasing carrier density has been observed, the maximum AH resistance is still far below quantum Hall resistance (h/e^2, ∼ 25.8 kΩ). This suggests that dissipative channels other than QAH edge states still dominate conduction.[40] To observe the QAH effect, we have further optimized MBE growth parameters of Cr-doped $(Bi,Sb)_2Te_3$ films, including substrate and surface condition, substrate temperature, film thickness, and material composition. These efforts lead to larger terrace size, reduced bulk carrier density, and higher mobility, which in turn result in larger AH resistance and lower longitudinal resistance. We have found that the amorphous Te capping layer we used to protect samples can significantly reduce the AH resistance when the sample is near the QAH regime, so that we have stopped using it. We have also applied a transport measurement facility equipped with a dilution refrigerator, which can provide a base temperature down to 30 mK and a magnetic field up to 18 T, to measure our samples. The above efforts finally lead to the experimental observation of the QAH effect.[48]

The optimized samples are 5-QL $Cr_{0.15}(Bi_{0.1}Sb_{0.9})_{1.85}Te_3$ films grown on 0.25-mm $SrTiO_3$ (111) substrates. To obtain more accurate ρ_{yx} and ρ_{xx} data, we manually cut the films into a Hall bar configuration for transport measurements. Figure 7(a) exhibits an example of such device. Such films have a Curie temperature of about 15 K, as shown in the temperature dependence of ρ_{yx} in Fig. 7(b).

Figures 8(a) and 8(c) show the magnetic field dependence of ρ_{yx} and ρ_{xx}, respectively, of $Cr_{0.15}(Bi_{0.1}Sb_{0.9})_{1.85}Te_3$ measured at $T = 30$ mK at different V_gs. Similar to the above result, the shape and coercivity of the ρ_{yx} hysteresis loops (Fig. 8(a)) vary little with V_g, thanks to the robust ferro-

magnetism mediated by the van Vleck mechanism.[39] In the magnetized states, ρ_{yx} is nearly independent of the magnetic field, suggesting perfect ferromagnetic ordering and charge neutrality of the sample. On the other hand, the AH resistance changes dramatically with V_g, with a maximum value of h/e^2 around $V_g = -1.5$ V. The magnetoresistance (MR) curves (Fig. 8(c)) exhibit the typical shape for a ferromagnetic material: two sharp symmetric peaks at the coercive fields.

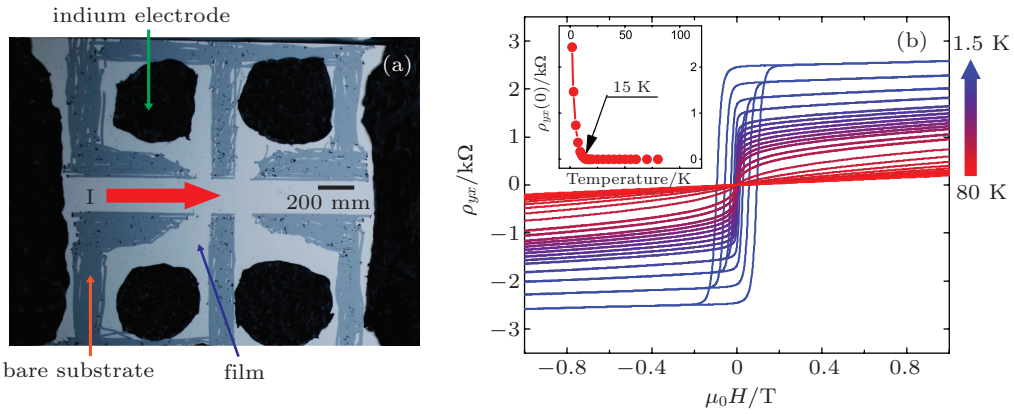

Fig. 7. (a) An optical image of a Hall bar device made from a 5-QL $Cr_{0.15}(Bi_{0.1}Sb_{0.9})_{1.85}Te_3$ film. (b) Magnetic field dependence of ρ_{yx} curves of the $Cr_{0.15}(Bi_{0.1}Sb_{0.9})_{1.85}Te_3$ film measured at different temperatures (from 80 K to 1.5 K). The inset shows the temperature dependence of zero field ρ_{yx}, which indicates a Curie temperature of ~ 15 K.[48]

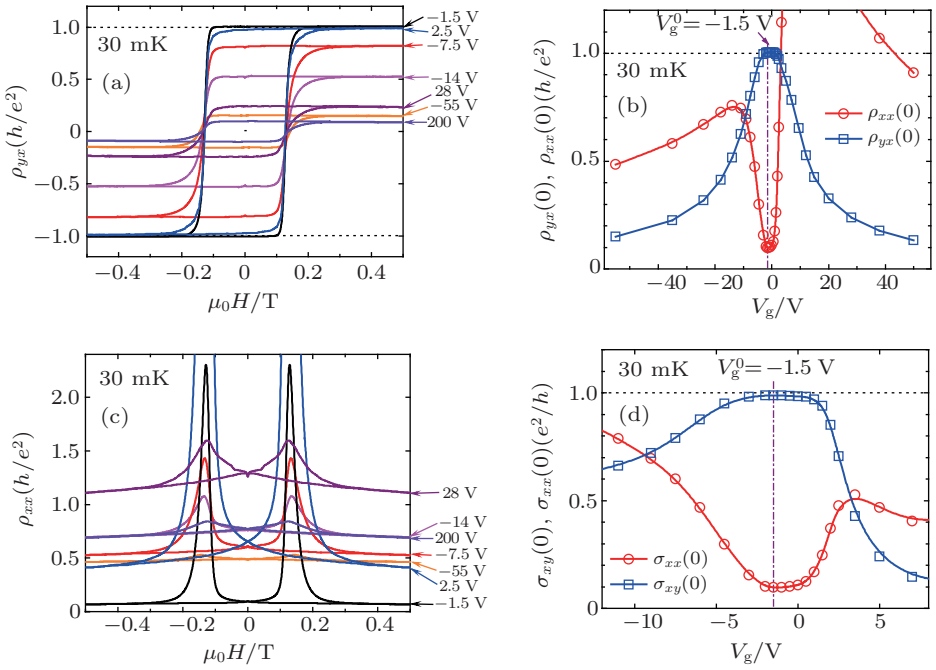

Fig. 8. The QAH effect measured at 30 mK. (a) Magnetic field dependence of ρ_{yx} at different V_gs. (b) Dependence of $\rho_{yx}(0)$ (empty blue squares) and $\rho_{xx}(0)$ (empty red circles) on V_g. (c) Magnetic field dependence of ρ_{xx} at different V_gs. (d) Dependence of $\sigma_{xy}(0)$ (empty blue squares) and $\sigma_{xx}(0)$ (empty red circles) on V_g. The vertical purple dashed–dotted lines in panels (b) and (d) indicate the V_g for V_g^0.[48]

The V_g dependences of $\rho_{yx}(0)$ and $\rho_{xx}(0)$ are plotted in Fig. 8(b). The most important observation here is that the zero field Hall resistance exhibits a distinct plateau with the quantized value h/e^2, which is centered around the gate voltage $V_g = -1.5$ V. This observation constitutes the discovery of the QAH effect. According to the OHE measurements, the maximum of ρ_{yx} is always located at the CNP (referred to as V_g^0 hereafter). Accompanying the quantization in ρ_{yx}, the longitudinal resistance $\rho_{xx}(0)$ exhibits a sharp dip down to $0.098h/e^2$. The $\rho_{yx}(0)/\rho_{xx}(0)$ ratio corresponds to a Hall angle of 84.4°. For comparison with theory, we transform $\rho_{yx}(0)$ and $\rho_{xx}(0)$ into sheet conductance via the relations: $\sigma_{xy} = \rho_{yx}/(\rho_{yx}^2 + \rho_{xx}^2)$ and $\sigma_{xx} = \rho_{xx}/(\rho_{yx}^2 + \rho_{xx}^2)$, and plot them in Fig. 8(d). Around V_g^0, $\sigma_{xy}(0)$ has a notable plateau at $0.987e^2/h$, whereas $\sigma_{xx}(0)$ has a dip down to $0.096e^2/h$, similar to the behavior of the corresponding resistances.

In addition to the observation of the QAH effect, the MR ratio $((\rho_{xx}(H_c) - \rho_{xx}(0))/\rho_{xx}(0))$ is dramatically enhanced at V_g^0 to a surprisingly large value of 2251% (Fig. 8(c)). The huge MR can also be understood in terms of the QAH phenomenology. In the magnetized QAH state, the existence of dissipationless edge state leads to a nearly vanishing ρ_{xx}. At the coercive field, the magnetization reversal of a QAH system leads to a quantum phase transition between two QH states via a highly dissipative phase with a large ρ_{xx}, though the exact process may be complex.[49] The huge MR thus reflects the distinct difference in transport properties between an ordinary insulator and a QAH insulator.

For a QH system, when the Fermi level lies in the gap between Landau levels, σ_{xy} reaches a plateau at e^2/h and σ_{xx} drops to zero. If the system contains non-localized dissipative conduction channels, σ_{xx} has a non-zero value, whereas σ_{xy} deviates slightly from the quantized plateau. For a QAH system, only one σ_{xy} plateau of e^2/h appears at zero field when the Fermi level is around the magnetically induced gap. The observations of $\sigma_{xy}(0) = e^2/h$ plateau and the dip in $\sigma_{xx}(0)$ near the charge neutral point in Fig. 8(d) thus agree with the theoretical prediction for a QAH system with residual dissipative channels. These channels are expected to vanish completely at zero temperature.

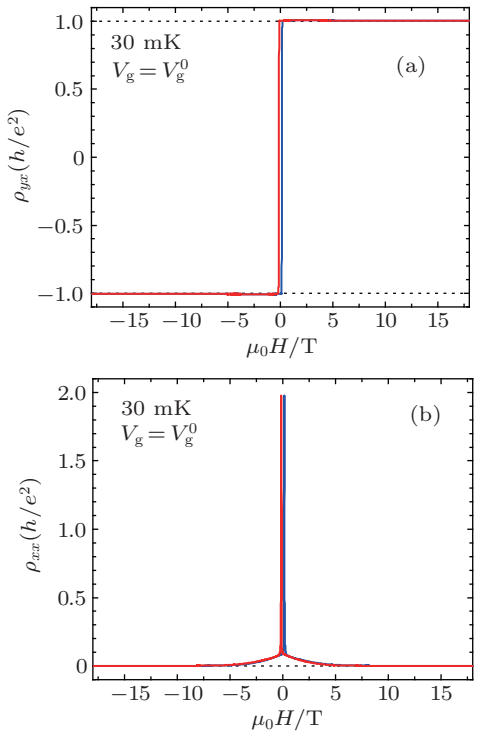

Fig. 9. The QAH effect under strong magnetic field measured at 30 mK. (a) Magnetic field dependence of ρ_{yx} at V_g^0. (b) Magnetic field dependence of ρ_{xx} at V_g^0. The blue and red lines in panels (a) and (b) indicate the data taken with increasing and decreasing fields, respectively.[48]

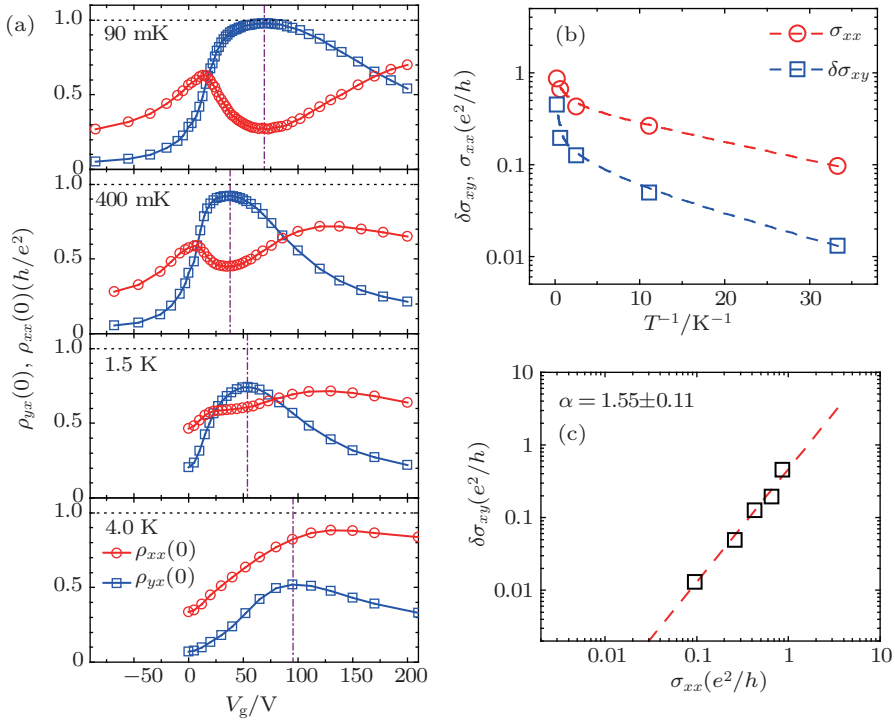

Fig. 10. Temperature dependence of the QAH effect. (a) V_g-dependent $\rho_{yx}(0)$ and $\rho_{xx}(0)$ measured at 90 mK, 400 mK, 1.5 K, and 4 K, respectively. The vertical purple dashed–dotted line indicates the V_g for V_g^0. The variation in the position and width of the $\rho_{yx}(0)$ peak at different temperatures results from the change in substrate dielectric properties induced by temperature and charging cycles. (b) Dependences of logarithmically scaled $\sigma_{xx}(0)$ (empty red circles) and $\delta\sigma_{xy}(0)$ (empty blue squares) at V_g^0 on inverse temperature. The dashed lines are a guide to the eye. (c) The relation between $\delta\sigma_{xy}(0)$ and $\sigma_{xx}(0)$ at V_g^0 in double logarithmic scale. The red dashed line indicates the fit with a power law $\delta\sigma_{xy} \propto \sigma_{xx}^{\alpha}$ with $\alpha \sim 1.55$.[48]

To confirm the QAH effect observed in Fig. 8, we apply a magnetic field, aiming to localize all possible dissipative states in the sample. Figures 9(a) and 9(b) display the magnetic field dependence of ρ_{yx} and ρ_{xx} of the same sample as in Fig. 8, respectively. Except for the large MR at H_c, increasing the field further suppresses ρ_{xx} toward zero. Above 10 T, ρ_{xx} vanishes completely, corresponding to a perfect QH state. It is noteworthy that the increase in ρ_{xx} from zero (above 10 T) to $0.098h/e^2$ (at zero field) is very smooth and ρ_{yx} remains at the quantized value h/e^2, which indicates that no quantum phase transition occurs, and the sample stays in the same QH phase as the field sweeps from 10 T to zero field. Therefore, the complete quantization above 10 T can only be attributed to the same QAH state at zero field.

The observation of the QAH effect is further supported by the behavior with varying temperatures. In Fig. 10(a), we show V_g dependencies of $\rho_{yx}(0)$ and $\rho_{xx}(0)$ measured at different temperatures in another sample with the same growth conditions. The $\rho_{yx}(0)$ always exhibits a single maximum, with the peak value considerably suppressed by increasing temperatures, accompanied by the disappearance of the dip in $\rho_{xx}(0)$. The $\sigma_{xx}(0)$ extracted from these measurements (in logarithmical scale, Fig. 10(b)) exhibits a temperature dependence similar to that in integer QH systems: the drop of σ_{xx} is at first rapid, resulting from the freezing of the thermal activation mechanism, and then becomes much slower when the temperature is below 1 K. It can be attributed to variable range hopping (VRH), but its exact mechanism remains unknown.[50] Similar to the QHE, zero field σ_{xx} is expected to decrease to zero at sufficiently low temperature. In Fig. 10(c) we plot the relation between $\sigma_{xx}(0)$ and $\delta\sigma_{xy}(0)$ ($\delta\sigma_{xy} = e^2/h - \sigma_{xy}$), which reflects the contribution of dissipative channels). A power law relation $\delta\sigma_{xy} \propto \sigma_{xx}^{\alpha}$ with $\alpha \sim 1.55$ is obtained. For a ferromagnetic insulator in the VRH regime, the AH conductivity is related to the longitudinal conductivity through $\sigma_{AH} = A\sigma_{xx}^{\alpha}$ (the power α is ~ 1.6, the prefactor A can be positive or negative depending on materials).[10] The above result can thus be qualitatively understood within the VRH framework.

5. Conclusion and outlook

We have reviewed how we experimentally approached the QAH effect from raw TI materials, from selection and preparation of materials to engineering of the electronic structures and properties. Eventually we observed AH resistance quantization and significant reduction of longitudinal resistance at zero field, as well as dissipationless transport aided by an external magnetic field, all of which unambiguously indicate the realization of the QAH effect. The non-zero longitudinal resistance at zero field and the extremely low temperature needed to reach AH resistance quantization imply that there are dissipative channels in the system that are difficult to be localized. One may try to reduce the film thickness and artificially introduce disorder in the film to promote electron localization so that zero field dissipationless transport may be realized at higher temperatures. This is crucial for possible applications of the QAH effect in the future.

The experimental observation of the QAH effect not only concludes the search of about 25 years for the QHE without Landau levels, but also lays the foundation for many other novel quantum phenomena predicted in TIs, e.g. topological magnetoelectric effect, image magnetic monopole effect, and Majorana bound states. Moreover, compared with the conventional QH effect, the QAH effect does not require high sample mobility. The samples showing the QAH effect in this work have mobility of less than 1000 $cm^2/V{\cdot}s$). Such robust QH states not only reflect the topological character of TIs but also make the QAH systems readily achievable in experiments. Because the realization of the QAH effect and dissipationless edge states does not require any magnetic field, the present work paves a path for developing low-power-consumption, topological quantum electronic and spintronic devices.

Acknowledgments

The authors would thank the collaborations and discussions with Chang Cui-Zu, Zhang Jin-Song, Feng Xiao, Shen Jie, Zhang Zuo-Cheng, Guo Ming-Hua, Li Kang, Ou Yun-Bo, Wei Pang, Wang Li-Li, Jia Jin-Feng, Ji Shuai-Hua, Dai Xi, Fang Zhong, Xie Xin-Cheng, Wang Jian, Zhang Sheng-Bai, Liu Chao-Xing, Zhu Bang-Fen, Duan Wen-Hui, Wu Jian, Tang Pei-Zhe, Shen Shun-Qing, Niu Qian, Qi Xiao-Liang, and Zhang Shou-Cheng.

References

[1] Dirac P A M 1947 *The Principles of Quantum Mechanics*, 3rd edn. (Oxford: Oxford University Press, USA)
[2] Klitzing K V, Dorda G and Peper M 1980 *Phys. Rev. Lett.* **45** 494
[3] Tsui D C, Stormer H L and Gossard A C 1982 *Phys. Rev. Lett.* **48** 1559
[4] Hall E H 1879 *Am. J. Math.* **2** 287
[5] Laughlin R B 1981 *Phys. Rev. B* **23** 5632
[6] Thouless D J, Kohmoto M, Nightingale M P and Nijs M D 1982 *Phys. Rev. Lett.* **49** 405
[7] Avron J E, Osadchy D and Seiler R, 2003 *Phys. Today* **56** 38
[8] Haldane F D M 1988 *Phys. Rev. Lett.* **61** 2015
[9] Hall E H 1881 *Philo. Mag.* **12** 157
[10] Nagaosa N, Sinova J, Onoda S, MacDonald A H and Ong N P 2010 *Rev. Mod. Phys.* **82** 1539
[11] Onoda M and Nagaosa N 2003 *Phys. Rev. Lett.* **90** 206601
[12] Kane C L and Mele E J 2005 *Phys. Rev. Lett.* **95** 226801
[13] Bernevig B A and Zhang S C 2006 *Phys. Rev. Lett.* **96** 106802
[14] Hasan M Z and Kane C L 2010 *Rev. Mod. Phys.* **82** 3045
[15] Qi X L and Zhang S C 2011 *Rev. Mod. Phys.* **83** 1057
[16] Bernevig B A, Hughes T L and Zhang S C 2006 *Science* **314** 1757

[17] König M, Wiedmann S, Brüne C, Roth A, Buhmann H, Molenkamp L W, Qi X L and Zhang S C 2007 *Science* **318** 766

[18] Liu C X, Hughes T L, Qi X L, Wang K and Zhang S C 2008 *Phys. Rev. Lett.* **100** 236601

[19] Knez I, Du R R and Sullivan G 2011 *Phys. Rev. Lett.* **107** 136603

[20] Fu L, Kane C L and Mele E J 2007 *Phys. Rev. Lett.* **98** 106803

[21] Fu L and Kane C L 2007 *Phys. Rev. B* **76** 045302

[22] Hsieh D, Qian D, Wray L, Xia Y, Hor Y S, Cava R J and Hasan M Z 2008 *Nature* **452** 970

[23] Hsieh D, Xia Y, Wray L, Qian D, Pal A, Dil J H, Osterwalder J, Meier F, Bihlmayer G, Kane C L, Hor Y S, Cava R J and Hasan M Z 2009 *Science* **323** 919

[24] Zhang H J, Liu C X, Qi X L, Dai X, Fang Z and Zhang S C 2009 *Nat. Phys.* **5** 438

[25] Xia Y, Qian D, Hsieh D, Wray L, Pal A, Lin H, Bansil A, Grauer D, Hor Y S, Cava R J and Hasan M Z 2009 *Nat. Phys.* **5** 398

[26] Chen Y L, Analytis J G, Chu J H, Liu Z K, Mo S K, Qi X L, Zhang H J, Lu D H, Dai X, Fang Z, Zhang S C, Fisher I R, Hussain Z and Shen Z X 2009 *Science* **325** 178

[27] Hsieh D, Xia Y, Qian D, Wray L, Dil J H, Meier F, Osterwalder J, Patthey L, Checkelsky J G, Ong N P, Fedorov A V, Lin H, Bansil A, Grauer D, Hor Y S, Cava R J and Hasan M Z 2009 *Nature* **460** 1101

[28] Qi X L, Wu Y S and Zhang S C 2006 *Phys. Rev. B* **74** 085308

[29] Liu C X, Qi X L, Dai X, Fang Z and Zhang S C 2008 *Phys. Rev. Lett.* **101** 146802

[30] Qi X L, Hughes T L and Zhang S C 2008 *Phys. Rev. B* **78** 195424

[31] Yu R, Zhang W, Zhang H J, Zhang S C, Dai X and Fang Z 2010 *Science* **329** 61

[32] Nomura K and Nagaosa N 2011 *Phys. Rev. Lett.* **106** 166802

[33] Li Y Y, Wang G, Zhu X G, Liu M H, Ye C, Chen X, Wang Y, He K, Wang L L, Ma X C, Zhang H J, Dai X, Fang Z, Xie X C, Liu Y, Qi X L, Jia J F, Zhang S C and Xue Q K 2010 *Adv. Mater.* **22** 4002

[34] Song C L, Wang Y L, Jiang Y P, Zhang Y, C. Chang C Z, Wang L, He K, Chen X, Jia J F, Wang Y, Fang Z, Dai X, Xie X C, Qi X L, Zhang S C, Xue Q K and Ma X 2010 *Appl. Phys. Lett.* **97** 143118

[35] Zhang Y, He K, Chang C Z, Song C L, Wang L L, Chen X, Jia J F, Fang Z, Dai X, Shan W Y, Shen S Q, Niu Q, Qi X L, Zhang S C, Ma X C, Xue Q K 2010 *Nat. Phys.* **6** 584

[36] Wang G, Zhu X, Wen J, Chen X, He K, Wang L L, Ma X C, Liu Y, Dai X, Fang Z, Jia J F and Xue Q K 2010 *Nano Res.* **3** 874

[37] Dietl T, Ohno H, Matsukura F, Cibert J and Ferrand D, 2000 *Science* **287** 1019

[38] Ohno H 1998 *Science* **281** 951

[39] Zhang J, Chang C Z, Tang P, Zhang Z, Feng X, Li K, Wang L L, Chen X, Liu C X, Duan W, He K, Xue Q K, Ma X C and Wang Y 2013 *Science* **339** 1582

[40] Chang C Z, Zhang J, Liu M, Zhang Z, Feng X, Li K, Wang L L, Chen X, Dai X, Fang Z, Qi X L, Zhang S C, Wang Y, He K, Ma X C and Xue Q K 2013 *Adv. Mater.* **25** 1065

[41] Chien Y J 2007 Ph. D. thesis of the University of Michigan, USA (http://deepblue.lib.umich.edu/handle/2027.42/57593)

[42] Hor Y S, Roushan P, Beidenkopf H, Seo J, Qu D, Checkelsky J G, Wray L A, Hsieh D, Xia Y, Xu S Y, Qian D, Hasan M Z, Ong N P, Yazdani A and Cava R J 2010 *Phys. Rev. B* **81** 195203

[43] Wang G, Zhu X G, Sun Y Y, Li Y Y, Zhang T, Wen J, Chen X, He K, Wang L L, Ma X C, Jia J F, Zhang S B and Xue Q K 2011 *Adv Mater.* **23** 2929

[44] Jiang Y P, Sun Y Y, Chen M, Wang Y L, Li Z, Song C L, He K, Wang L L, Chen X, Xue Q K, Ma X C and Zhang S B 2012 *Phys. Rev. Lett.* **108** 066809

[45] Zhang J, Chang C Z, Zhang Z, Wen J, Feng X, Li K, Liu M, He K, Wang L L, Chen X, Xue Q K, Ma X and Wang Y 2011 *Nat. Commun.* **2** 574

[46] Benia H M, Lin C, Kern K and Ast C R 2011 *Phys. Rev. Lett.* **107** 177602

[47] Chen J, Qin H J, Yang F, Liu J, Guan T, Qu F M, Zhang G H, Shi J R, Xie X C, Yang C L, Wu K H, Li Y Q and Lu L 2010 *Phys. Rev. Lett.* **105** 176602

[48] Chang C Z, Zhang J, Feng X, Shen J, Zhang Z, Guo M, Li K, Ou Y, Wei P, Wang L L, Ji Z Q, Feng Y, Ji S, Chen X, Jia J F, Dai X, Fang Z, Zhang S C, He K, Wang Y, Lu L, Ma X C and Xue Q K 2013 *Science* **340** 167

[49] Checkelsky J G, Ye J, Onose Y, Iwasa Y and Tokura Y 2012 *Nat. Phys.* **8** 729

[50] Jeckelmann B and Jeanneret B 2001 *Rep. Prog. Phys.* **64** 1603